

Performance Optimization and Instability Study in Ring Cavity Quantum Cascade Lasers

Mahdi Moradinasab, *Student Member, IEEE*, Mahdi Pourfath, *Member, IEEE*,
and Hans Kosina, *Member, IEEE*

Abstract—An optimization study of quantum cascade lasers (QCLs) considering the laser instability condition is performed. To model current transport, the Pauli master equation is solved using a Monte Carlo approach. The effects of saturable absorber and pumping strength on the instability threshold are investigated. A particle swarm optimization algorithm is applied to increase the laser optical gain. A large optical gain below the instability threshold is achieved for optimized QCL designs. To analyze the optimized structure, a numerical calculation based on the Maxwell–Bloch equations is performed. The results indicate side-mode instabilities due to Risken–Nummedal–Graham–Haken-like instability.

Index Terms—Particle swarm optimization, Monte Carlo simulation, quantum cascade laser, mode locked lasers, saturable absorber.

I. INTRODUCTION

QUANTUM cascade lasers (QCLs) are the most prominent and compact coherent light sources in the wavelength range from 3.5 to 20 μm . Remarkable design degrees of freedom make QCLs a unique candidate to serve as a semiconductor source of ultrashort pulses in the mid-infrared (MIR) region [1]–[3]. Ultrashort pulses which are generated in QCL media have been employed for various applications, such as non-linear frequency conversion [4], [5], high-speed free space communication [6], and trace gas detection [7].

The most common technique for generation of ultrashort pulses is mode locking which is realized either by an internal mechanism (passive mode locking) or an external one (active mode locking) [8]. Active modelocking does not lead to ultrashort pulses, because the frequency of modulation cannot be raised arbitrarily while a passive saturable absorber is much more effective in ultrashort pulse generation [9]. In lasers with a relatively long gain recovery time compared to the cavity round-trip time, the instability caused by a saturable absorber (SA) can often lead to passive mode locking [9].

Manuscript received July 28, 2014; revised October 24, 2014; accepted November 17, 2014. Date of publication November 20, 2014; date of current version December 10, 2014. This work was supported by the Austrian Science Fund under Grant F2514.

M. Moradinasab and H. Kosina are with the Institute for Microelectronics, Technische Universität Wien, Vienna A-1040, Austria (e-mail: moradinasab@iue.tuwien.ac.at; kosina@iue.tuwien.ac.at).

M. Pourfath is with the School of Electrical and Computer Engineering, University of Tehran, Tehran 14395-515, Iran, and also with the Institute for Microelectronics, Technische Universität Wien, Vienna A-1040, Austria (e-mail: pourfath@ut.ac.ir).

Color versions of one or more of the figures in this paper are available online at <http://ieeexplore.ieee.org>.

Digital Object Identifier 10.1109/JQE.2014.2373171

Because of ultra-fast tunneling and inter-subband transitions, QCLs, unlike conventional semiconductor lasers, have a gain recovery (in the order of picoseconds) faster than the cavity round trip time. Therefore, SA dominated self-mode locking seems impossible in typical QCLs. However, as reported in Ref. [10], under these conditions the elusive Risken–Nummedal–Graham–Haken (RNGH)-like instability can be observed in QCLs. It is demonstrated that fast gain recovery of QCLs exhibits two kinds of instabilities in the multi-mode regime: the RNGH-like instability and one associated with spatial hole burning (SHB) [11].

The active mode locking in QCLs is strongly limited by SHB which leads to a proliferation of modes with random phases and destroys coherence [8].

In this work we investigate performance optimization and passive mode locking caused by a saturable absorber in a ring cavity QCL in which the SHB instability does not occur because of the absence of standing waves. Performance optimization of QCLs has achieved significant progress in recent years [12]–[14]. The performance of QCLs can be improved by optimizing the epitaxial growth, fabrication process, and active region design [15]–[17]. The latter is important in order to insure efficient carrier injection in the upper lasing state and carrier extraction out of the lower lasing state [14].

So far, optimization techniques proposed to design QCL structures are based on genetic algorithms [12], [14], [18], [19]. A multi-variable multi-objective optimization algorithm for terahertz QCLs is presented in [13]. In [12] and [14], a technique to design quantum cascade structures in the mid-infrared is proposed. Particle swarm optimization (PSO) [20] is as an alternative to traditional evolutionary algorithms. It attempts to mimic the goal-seeking behavior of biological swarms. In PSO, a possible solution of the optimization problem is represented as a particle, and the algorithm operates in an iterative manner. Unlike traditional evolutionary algorithms, particles in PSO do not perform the operation of genetic recombination between particles, but they work individually with social behavior in swarms. PSO has some attractive characteristics. In particular, it has memories, so that knowledge of good solutions can be retained by all particles (solutions). This method has been successfully used to solve many discontinuous and complex problems with good results [21], [22].

In this paper, we perform an optimization study of ring cavity QCLs considering the laser instability condition. Laser design parameters, including the barrier and well thicknesses and applied electric field, are modified for maximizing laser

gain under a desired instability condition. Passive mode locking with saturable absorber is investigated for the optimized QCLs. The effects of saturable absorber and pumping strength on the instability characteristics are studied. A large optical gain below the instability threshold is achieved for optimized QCL designs. A numerical calculation based on the Maxwell-Bloch equations is performed to analyze the optimized structure. This paper is organized as follows:

Sec. II describes the optimization method and the models used. In Sec. III, the simulation results for the optimized structure are presented and discussed. Concluding remarks are presented in Sec. IV.

II. METHOD AND MODELS

Because of the large number of involved design parameters, performance improvement of QCLs requires a systematic multi-objective optimizer in conjunction with a simulation tool which has a good balance between computational speed and physical accuracy.

Various approaches such as rate equations [23], [24], Monte-Carlo simulations [25], density matrix methods [26], and the non-equilibrium Green's function formalism (NEGF) [27], [28] have been developed for the simulation of QCLs.

The simplest models, based entirely on scattering and neglecting coherence effects, require a fewer number of material parameters and are generally able to predict the threshold current density but not the light-current or current-voltage characteristics [29]. Pure quantum mechanical models based on NEGF or the density matrix have been used as rigorous approaches to capture the QCL physics. The NEGF theory takes into account incoherent scattering with phonons, impurities, and rough interfaces as well as electron-electron scattering in the Hartree approximation [27]. Unfortunately, the inherently high computational costs of full quantum mechanical models render them unfeasible for optimization purposes [27].

To study electronic transport in QCL, we employ the Pauli-master equation solved by the Monte-Carlo method [30]. In this semi-classical approach, the transport is modeled via scattering between energy states, including acoustic and optical deformation potential and polar optical electron-phonon scattering as well as alloy, inter-valley, and interface roughness scattering. Accurate results along with a relatively low computational cost render this approach as a good candidate for optimization studies.

The PSO is an iterative method which initializes a number of vectors (called particles) randomly within the search space of the objective function. These particles are collectively known as the swarm. Each particle represents a potential solution to the problem expressed by the objective function. During each time step the objective function is evaluated to establish the fitness of each particle using its position as input. Fitness values are used to determine which positions in the search space are better than others. Particles are then made to fly through the search space being attracted to both their personal best position as well as the best position found by

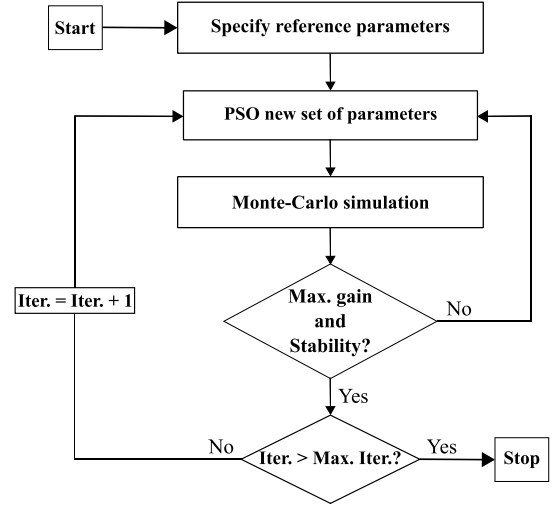


Fig. 1. The algorithm of the developed optimization framework.

the swarm so far [31]. The particles are *flown* through the search space by updating the position of the i^{th} particle at time step k according to the following equation [31]:

$$x_i^{k+1} = x_i^k + v_i^k, \quad (1)$$

where x_i^k and v_i^k are vectors representing the current position and velocity, respectively. Assuming particles of dimension $j \in 1 \dots n$, the velocity updates are governed by the following equation [32]:

$$v_{i,j}^{k+1} = \omega v_{i,j}^k + c_1 r_{1,j} (y_{i,j} - x_{i,j}^k) + c_2 r_{2,j} (\hat{y}_j - x_{i,j}^k), \quad (2)$$

where $0 < \omega < 1$ is an inertia weight determining how much of the particle's previous velocity is preserved, c_1 and c_2 are two positive acceleration constants, $r_{1,j}$ and $r_{2,j}$ are two uniform random sequences sampled from $U(0, 1)$, y_i is the personal best position found by the i^{th} particle and \hat{y} is the best position found by the entire swarm so far. The following relation should hold in order for the PSO to converge [31]:

$$\frac{c_1 + c_2}{2} - 1 < \omega. \quad (3)$$

However, the standard PSO is not guaranteed to converge on a local extremum, but most of the recent PSO algorithms converge to the global optimum.

Employing a Pauli master equation-based description of electronic transport in QCLs along with the multi-objective PSO strategy, a framework is developed for maximizing laser gain with simultaneous desirable instability operation. In this framework one starts from a reference design. In the next iterations the well and barrier thicknesses and the applied electric field are modified until maximum gain and laser operation below the instability threshold are achieved. The analytical linear stability model introduced in Ref.[11] is employed to analyze the instability threshold of the studied QCL. In this model, the criteria for RNGH instability is expressed in terms of the parametric gain $g(\Omega)$ as a function of the resonance

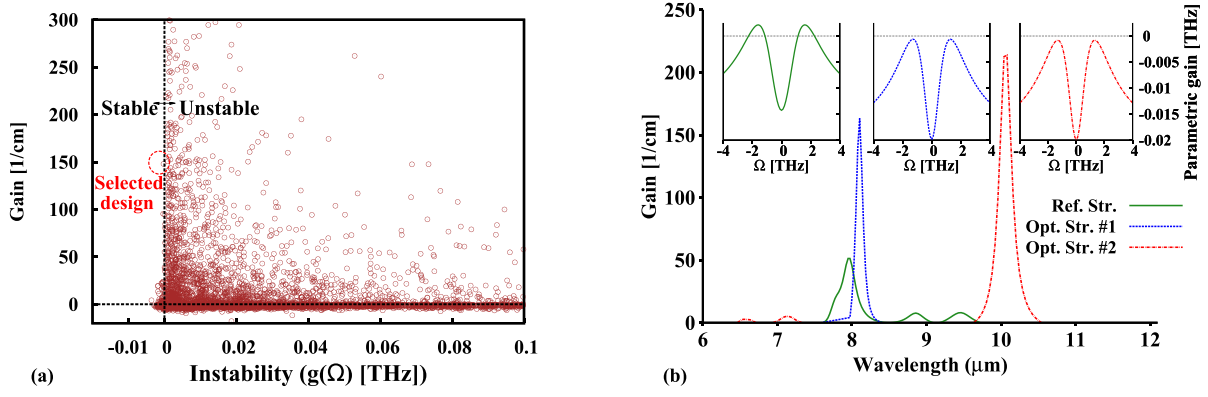


Fig. 2. (a) The PSO results for different particles searching the search space and (b) gain spectra and instability thresholds for the reference and optimized structures.

frequency Ω

$$g(\Omega) = -\frac{c}{2n} \text{Re} \left[l_0 \frac{(\Omega T_1 + i)\Omega T_2 - 2(p_f - 1)}{(\Omega T_1 + i)(\Omega T_2 + i) - (p_f - 1)} + \frac{\gamma \hbar^2 (p_f - 1)}{\mu^2 T_1 T_2} \frac{(\Omega T_1 + i)(3\Omega T_2 + 2i) - 4(p_f - 1)}{(\Omega T_1 + i)(\Omega T_2 + i) - (p_f - 1)} \right], \quad (4)$$

where p_f is the pumping factor, T_1 is the gain recovery time, T_2 is the dephasing time, l_0 is the linear cavity loss, μ is the matrix element of the lasing transition, and γ is the SA coefficient. The derivation of Eq.4 is presented in detail in the appendix. Based on this analysis each mode, which is identified by the resonance frequency Ω , is stable if the parametric gain is negative, otherwise it is unstable. At each iteration of the optimization loop, for a set of geometrical parameters and the applied electric field, the parameters T_1 , T_2 , and μ are extracted and the parametric gain (Eq. 4) is evaluated. If the stability condition is not satisfied, a new set of parameters is selected for the next iteration. The flow chart of the developed framework is described in Fig. 1.

III. RESULTS AND DISSCUSION

We consider the laser gain as a figure of merit and define the instability criterion to satisfy stability conditions. Using the scattering times and calculating the dipole matrix elements, the gain coefficient g can be estimated for each structure as [33]:

$$g = \tau_3 \left(1 - \frac{\tau_2}{\tau_{32}} \right) \frac{4\pi e \mu^2}{\lambda_0 \epsilon_0 n_{\text{eff}} L_p} \frac{1}{2\gamma_{32}}, \quad (5)$$

where λ_0 is the wavelength in vacuum, ϵ_0 the vacuum dielectric constant, e the elementary charge, n_{eff} the effective refractive index of the mode, L_p the length of one period including active region and injector, and $2\gamma_{32}$ is the full width at half maximum value of the luminescence spectrum.

In fact, the optimization framework changes the geometrical parameters which affect the lifetimes and matrix elements. Simulation results indicate that two key parameters modified in optimized designs are the matrix element μ and the upper laser level lifetime τ_3 ($\approx T_1$ in Eq. 5). The gain coefficient

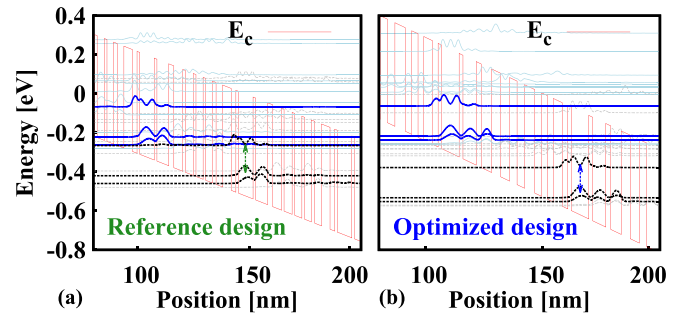


Fig. 3. The conduction band diagram and the wavefunctions of (a) the reference design and (b) the optimized structure. The lasing subbands are indicated with bold solid/bold dashed lines.

increases with these two parameters (see Eq. 5). The parameters of the reference design are mentioned in Ref. [33]. The layer sequence of the $\text{In}_{0.52}\text{Al}_{0.48}\text{As}/\text{In}_{0.53}\text{Ga}_{0.47}\text{As}$ for the optimized structure, starting with the injection barrier is: **3.74/2.36/1.50/7.45/1.63/5.63/2.15/4.43/3.86/3.85/3.15/3.18/4.40/2.79/2.67/2.46** nm, where the barrier layers are bold and underlined layers are n-doped with Si at $2 \times 10^{17} \text{cm}^{-3}$.

Figure 2(a) shows the PSO results for different particles searching the search space. Most points (samples) are located at the right-side of vertical dashed-line which represent unstable laser operation. The samples at the left-side of vertical dashed-line and upper of the horizontal dashed-line are the ones we are looking for.

The instability threshold behavior and gain spectrum for the reference design and two obtained optimized designs are exhibited in Fig. 2(b). The first structure is optimized at the same wavelength as the reference design and the second one is optimized at a higher wavelength but with a larger gain. Our developed framework has the advantage of optimizing the reference structure for a specific wavelength. We focus on the first optimized structure which has the same wavelength as the reference structure.

The conduction band diagram and the associated wave-functions of the reference design and optimized structure is shown in Fig. 3. As shown in Fig. 3(b), the active region of the optimized structure is a three-well (3QW) vertical-transition design which provides high optical gain

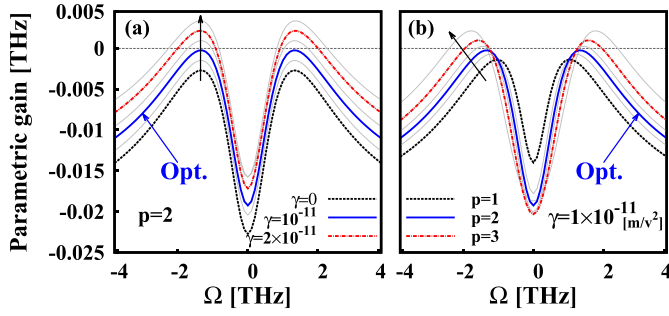


Fig. 4. The parametric gain $g(\Omega)$ as a function of the resonance frequency Ω at various (a) SA coefficients and (b) pumping strengths.

TABLE I
THE PARAMETERS USED FOR THE INSTABILITY
ANALYSIS OF THE OPTIMIZED STRUCTURE

T_1	Gain recovery time	0.46ps
T_2	Dephasing time	0.06 ps
μ	Matrix element of lasing transition	2.44×10^{-9} m
n	Refractive index	3.25
l_0	Linear cavity loss	500 m ⁻¹
L	Cavity length	6×10^{-3} m
γ	Saturable absorber coefficient	10^{-11} m/V ²

and concomitant robustness for laser action. The upper laser level for the optimized structure is delocalized which results in an increase at the upper laser level lifetime τ_3 and the laser gain consequently (see Eq. 5). The parameters extracted for the instability analysis of the optimized structure are shown in Table I. Fig. 4(a) indicates that the instability threshold decreases uniformly with the SA coefficient, for example $\gamma \geq 3$ m/V² triggers the instability for the optimized structure at a relatively low pumping strength ($p_f = 2$). As reported in [11], a saturable absorber always favours a multimode regime to a single mode one, which explains why the instability threshold decreases with γ in the optimized design. As discussed later, this instability results in Rabi sidebands around the cw lasing frequency.

The parametric gain of the optimized structure at various pumping strengths is shown in Fig. 4(b). A larger pumping strength broadens the instability characteristics and decreases the instability threshold. The results are consistent with previous works [11].

The active-region of the current studied QCL is based on a 3QW vertical-transition design which is separated from the injection/relaxation region by a tunneling barrier [33]. Here, we present the optimization results for a reference QCL with a superlattice (SL) active-region [34].

The instability characteristics for the 3QW and SL active-regions are compared in Fig. 5(a). Because of the larger matrix element (μ) and longer upper laser state lifetime (τ_3), which is approximately equal to the gain recovery time (T_1), the SL active-region QCL indicates more stable operation and higher instability threshold (see Fig. 5(a)). However, as we mentioned earlier, the matrix element and lifetimes of the lasing transition, which are the key parameters in linear stability analysis, are proportional to optical gain (see Eq. 5).

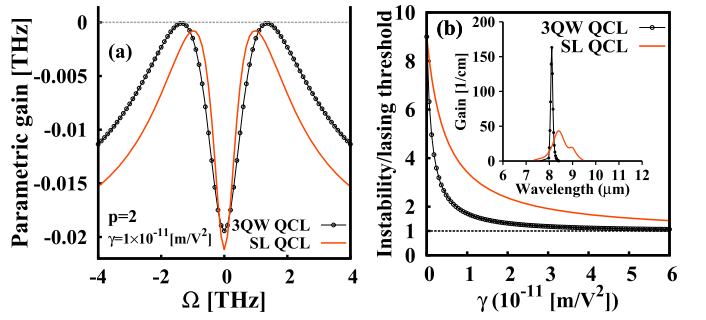


Fig. 5. (a) The parametric gain $g(\Omega)$ as a function of the resonance frequency Ω . (b) The pumping ratio p_f at which the RNGH instability sets in as a function of the SA coefficient. Inset: Optical gain spectra obtained for two optimized active-region QCLs.

As it is indicated in the inset of Fig. 5(b), 3QW QCL exhibits larger optical gain at nearly the same wavelength. The optical gain of 3QW structure is maximized by delocalizing the lasing states which increases the lifetimes (τ_3) and (τ_2). Because of the bound states in SL active-region, there is no significant lifetime variation, however, due to the larger matrix element, better instability condition is achieved.

The linear stability analysis, however, predicts only the instability threshold and does not describe the dynamics of the laser. To investigate the dynamics of QCLs above the instability threshold, the Maxwell-Bloch equations are solved numerically. The effect of the SA is modeled as the intensity-modulated optical field amplitude in the standard Maxwell-Bloch equations [9]:

$$\partial_t E = -\frac{c}{n} \partial_z E - \frac{c}{n} \frac{i\mu P}{\hbar l_0 D_{th}} - \frac{c}{2n} (l_0 - \bar{\gamma} |E|^2) E, \quad (6)$$

$$\partial_t P = \frac{i\mu}{2\hbar} DE - \frac{P}{T_2}, \quad (7)$$

$$\partial_t D = \frac{D_p - D}{T_1} + \frac{i\mu}{\hbar} (E^* P - c.c.). \quad (8)$$

E and P are the envelopes of the normalized electric field and polarization, respectively, D represents the normalized average population inversion, D_p is the normalized steady-state population inversion, D_{th} is the lasing threshold value of D_p for $\gamma = 0$, proportional to the pumping factor p_f ($p_f \geq 1$), l_0 is the linear cavity loss, and $\bar{\gamma} = \hbar^2 \gamma / \mu^2$.

We employ a finite-difference discretization scheme to find the evolution of electric field, polarization, and population inversion in the spatial and time domain. A periodic boundary condition is applied to model a ring cavity.

The number of mesh points play an important role in preventing unreasonable results and achieving consistency. There should be large enough number of grids to make sure there is not any un-inspected variation. The $x-t$ plane is divided into a $m \times n$ mesh points. The number of mesh points are $m = 500$ and $n = 10^5$ which correspond to the grid sizes of $\Delta x = 12 \mu\text{m}$ and $\Delta t = 120$ fs, respectively. The periodic boundary conditions for the dynamical variables of the QCL (electric field E , polarization P , and population inversion D) are $E(0, n) = E(L, n)$, $P(0, n) = P(L, n)$, and $D(0, n) = D(L, n)$.

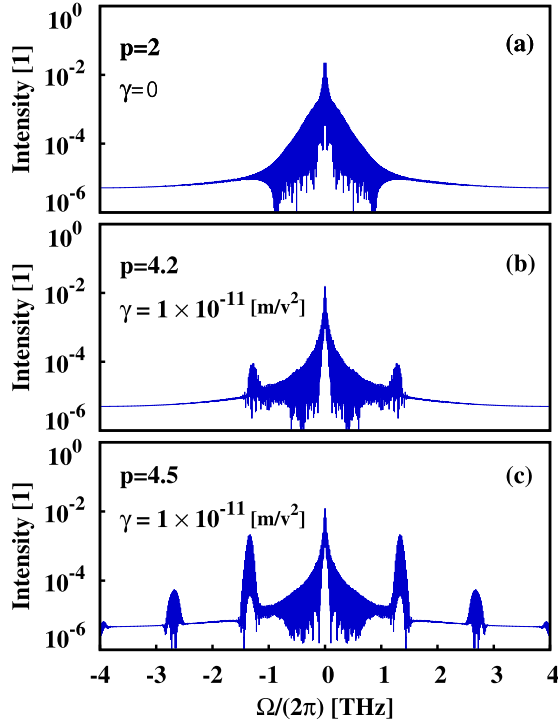


Fig. 6. The spectra of the optical intensity in logarithmic scale for (a) no SA coefficient (b) SA coefficient at the instability threshold, and (c) SA coefficient at the instability threshold and a larger pumping factor.

For the parameters corresponding to the optimized QCL including the SA, the lasing instability appears as the rise of the side modes with the increase of the SA coefficient. The energy in the Rabi sidebands can change either discontinuously or continuously at the RNGH instability threshold [11]. In lasers with slow gain recovery time, the transition in the Rabi sidebands is discontinuous [35], however, because of the fast gain recovery time in QCLs, Rabi sidebands continuously grow around the central cw mode, see Fig. 6. Furthermore, more Rabi side modes appear with the increase of the pumping strength.

IV. CONCLUSION

An optimization framework is developed to maximize the gain of the laser with regard to the instability threshold. Optimized structures exhibit a larger gain and operate below the instability threshold in comparison with the reference design. The dynamics of the optimized design above the threshold instability is numerically analyzed by solving Maxwell-Bloch equations. The results indicate that the lasing instability, which appears as side modes in the optical spectrum, occurs with the increase of the SA coefficient even at low pumping strength. The increase of the SA coefficient and pumping strength reduce the instability threshold whereas the instability characteristics is broadened by the pumping strength.

The developed optimization framework is flexible enough to incorporate other criteria such as wavelength specification, sheet doping density, strain, and so forth performing a comprehensive study. This optimization scheme and the presented

results are useful for further advancement in designing QCLs operating under a desirable instability conditions.

APPENDIX LINEAR STABILITY ANALYSIS

The standard Maxwell-Bloch equations with a SA added can be rewritten as [9]:

$$\partial_t E = -\frac{c}{n} \partial_z E - \frac{c}{n} \frac{i\mu P}{\hbar l_0 D_{th}} - \frac{c}{2n} (l_0 - \bar{\gamma} |E|^2) E, \quad (9)$$

$$\partial_t P = \frac{i\mu}{2\hbar} DE - \frac{P}{T_2}, \quad (10)$$

$$\partial_t D = \frac{D_p - D}{T_1} + \frac{i\mu}{\hbar} (E^* P - c.c.). \quad (11)$$

The dynamics of a two-level QCL gain medium with ring cavity can be described using the Maxwell-Bloch equations. After transformation of the variables, the Maxwell-Bloch equations can be simplified to:

$$\partial_t E = -\frac{c}{n} \partial_z E - \frac{c}{n} i P - \frac{c}{2n} (l_0 - \bar{\gamma} |E|^2) E, \quad (12)$$

$$\partial_t P = -\frac{i}{2} DE - \frac{P}{T_2}, \quad (13)$$

$$\partial_t D = \frac{p_f l_0}{T_1 T_2} - \frac{D}{T_1} + i (E^* P - c.c.). \quad (14)$$

To proceed with the linear stability analysis, we express each of the variables as the sum of the steady-state value and the small perturbations δE , δP , and δD .

The steady state solution can be found by setting the left-hand sides of the Eqs. (12)-(14) to zero. The steady state solutions has the form $E = \bar{E}$, $P = \bar{P}$, and $D = \bar{D}$ are constants in time and space satisfying:

$$\bar{D} = \frac{l_0}{T_2} - \frac{\bar{\gamma} \bar{E}^2}{T_2}, \quad (15)$$

$$\bar{P} = \frac{i}{2} (l_0 - \bar{\gamma} \bar{E}^2) \bar{E}, \quad (16)$$

$$p_f + 1 = \left(1 - \frac{\bar{\gamma} \bar{E}^2}{l_0}\right) (1 + \bar{E}^2 T_1 T_2). \quad (17)$$

The resulting equations regarding the fluctuations are

$$\partial_t \delta P_I = \frac{1}{2} (\bar{D} \delta E_R + \delta D \bar{E}) - \frac{\delta P_I}{T_2}, \quad (18)$$

$$\partial_t \delta D = -T_2 \bar{D} \bar{E} \partial E_R - 2 \bar{E} \delta P_I - \frac{\delta D}{T_1}, \quad (19)$$

$$\partial_t \delta E_R = \frac{c}{n} \left[-\partial_z \delta E_R + \delta P_I - (l_0 - 3\bar{\gamma} \bar{E}^2) \frac{\delta E_R}{2} \right], \quad (20)$$

$$\partial_t \delta P_R = -\frac{1}{2} \bar{D} \delta E_I - \frac{\delta P_R}{T_2}, \quad (21)$$

$$\partial_t \delta E_I = \frac{c}{n} \left[-\partial_z \delta E_I - \delta P_R - (l_0 - \bar{\gamma} \bar{E}^2) \frac{\delta E_I}{2} \right]. \quad (22)$$

The two sets of equations, (18)-(20) and (21)-(22), are decoupled, and translationally invariant. Thus their eigenfunctions are the plane waves [11]. Therefore, it holds $\delta P_I(z, t) = \delta P_I(t) e^{ikz}$, and similarly for δD and δE_R . The stability of the

cw solution is determined by the eigenvalues of the matrix

$$\begin{pmatrix} -T_2^{-1} & \frac{1}{2T_2}(l_0 - \bar{\gamma}\bar{E}^2) & \frac{1}{2}\bar{E} \\ \frac{c}{n} & \frac{c}{n}\left(-\frac{1}{2}l_0 + \frac{3}{2}\bar{\gamma}\bar{E}^2 - ik\right) & 0 \\ -2\bar{E} & \bar{\gamma}\bar{E}^3 - l_0\bar{E} & -T_2^{-1} \end{pmatrix}. \quad (23)$$

If all eigenvalues have a negative real part, the cw solution is stable.

For $l_0 = 0$ and $\bar{\gamma} = 0$, the eigenvalue with the greatest real part is $\lambda_0(K) = -ick/n$. Putting $\lambda(K) = \lambda_0(K) + \lambda_1(K)$ into the characteristic polynomial of M and equating the parts which are first order in l_0 , $\bar{\gamma}$, and $\lambda_1(K)$, one arrives at

$$\lambda_{\max} = -i\Omega - \frac{l_0c}{2n} \frac{(\Omega T_1 + i)\Omega T_2 - 2(p_f - 1)}{(\Omega T_1 + i)(\Omega T_2 + i) - (p_f - 1)} + \frac{\gamma \hbar^2(p_f - 1)}{\mu^2 T_1 T_2} \frac{(\Omega T_1 + i)(3\Omega T_2 + 2i) - 4(p_f - 1)}{(\Omega T_1 + i)(\Omega T_2 + i) - (p_f - 1)}, \quad (24)$$

where $p_f = D_p/D_{th}$ and $\Omega = kc/n$. Taking the real part of Eq. 24 one obtains Eq. 4.

REFERENCES

- [1] C. Y. Wang *et al.*, "Mode-locked pulses from mid-infrared quantum cascade lasers," *Opt. Exp.*, vol. 17, no. 15, pp. 12929–12943, 2009.
- [2] Y. Yao, A. J. Hoffman, and C. F. Gmachl, "Mid-infrared quantum cascade lasers," *Nature Photon.*, vol. 6, no. 7, pp. 432–439, 2012.
- [3] J. R. Freeman, J. Maysonnave, H. E. Beere, D. A. Ritchie, J. Tignon, and S. S. Dhillon, "Electric field sampling of modelocked pulses from a quantum cascade laser," *Opt. Exp.*, vol. 21, no. 13, pp. 16162–16169, 2013.
- [4] J. M. Dudley, G. Genty, and S. Coen, "Supercontinuum generation in photonic crystal fiber," *Rev. Modern Phys.*, vol. 78, no. 4, pp. 1135–1184, 2006.
- [5] E. A. Gibson *et al.*, "Coherent soft X-ray generation in the water window with quasi-phase matching," *Science*, vol. 302, no. 5642, pp. 95–98, 2003.
- [6] R. Paiella *et al.*, "Monolithic active mode locking of quantum cascade lasers," *Appl. Phys. Lett.*, vol. 77, no. 2, pp. 169–171, 2000.
- [7] R. Paiella *et al.*, "Self-mode-locking of quantum cascade lasers with giant ultrafast optical nonlinearities," *Science*, vol. 290, no. 5497, pp. 1739–1742, 2001.
- [8] V.-M. Gkortsas *et al.*, "Dynamics of actively mode-locked quantum cascade lasers," *Opt. Exp.*, vol. 18, no. 13, pp. 13616–13630, 2010.
- [9] H. A. Haus, "Mode-locking of lasers," *IEEE J. Sel. Topics Quantum Electron.*, vol. 6, no. 6, pp. 1173–1185, Nov./Dec. 2000.
- [10] C. Y. Wang *et al.*, "Coherent instabilities in a semiconductor laser with fast gain recovery," *Phys. Rev. A*, vol. 75, no. 3, p. 031802, 2007.
- [11] A. Gordon *et al.*, "Multimode regimes in quantum cascade lasers: From coherent instabilities to spatial hole burning," *Phys. Rev. A*, vol. 77, no. 5, p. 053804, 2008.
- [12] A. Daničić, J. Radovanović, V. Milanović, D. Indjin, and Z. Ikonić, "Optimization and magnetic-field tunability of quantum cascade laser for applications in trace gas detection and monitoring," *J. Phys. D, Appl. Phys.*, vol. 43, no. 4, p. 045101, 2010.
- [13] M. T. Arafat, N. Islam, S. Roy, and S. Islam, "Performance optimization for terahertz quantum cascade laser at higher temperature using genetic algorithm," *Opt. Quantum Electron.*, vol. 44, no. 15, pp. 701–715, 2012.
- [14] A. Bismuto, R. Terazzi, B. Hinkov, M. Beck, and J. Faist, "Fully automatized quantum cascade laser design by genetic optimization," *Appl. Phys. Lett.*, vol. 101, no. 2, p. 021103, 2012.
- [15] M. Beck *et al.*, "Continuous wave operation of a mid-infrared semiconductor laser at room temperature," *Science*, vol. 295, no. 5553, pp. 301–305, 2002.
- [16] Y. Bai, N. Bandyopadhyay, S. Tsao, S. Slivken, and M. Razeghi, "Room temperature quantum cascade lasers with 27% wall plug efficiency," *Appl. Phys. Lett.*, vol. 98, no. 18, p. 181102, 2011.
- [17] R. Maulini, A. Lyakh, A. Tsekoun, R. Go, and C. K. N. Patel, "High average power uncooled mid-wave infrared quantum cascade lasers," *Electron. Lett.*, vol. 47, no. 6, pp. 395–397, 2011.
- [18] P. A. Sanchez-Serrano, D. Wong-Campos, S. Lopez-Aguayo, and J. C. Gutiérrez-Vega, "Engineering of nondiffracting beams with genetic algorithms," *Opt. Lett.*, vol. 37, no. 24, pp. 5040–5042, 2012.
- [19] D. Gagnon, J. Dumont, and L. J. Dubé, "Multiobjective optimization in integrated photonics design," *Opt. Lett.*, vol. 38, no. 13, pp. 2181–2184, 2013.
- [20] R. Poli, J. Kennedy, and T. Blackwell, "Particle swarm optimization," *Swarm Intell.*, vol. 1, no. 1, pp. 33–57, 2007.
- [21] F. Grimalaccia, M. Mussetta, and R. E. Zich, "Genetical swarm optimization: Self-adaptive hybrid evolutionary algorithm for electromagnetics," *IEEE Trans. Antennas Propag.*, vol. 55, no. 3, pp. 781–785, Mar. 2007.
- [22] R.-Y. Wang, W.-P. Lee, and Y.-T. Hsiao, "A new cooperative PSO approach for the optimization of multimodal functions," in *Proc. World Congr. Eng. (WCE)*, 2012, pp. 418–424.
- [23] D. Indjin, P. Harrison, R. W. Kelsall, and Z. Ikonić, "Self-consistent scattering theory of transport and output characteristics of quantum cascade lasers," *J. Appl. Phys.*, vol. 91, no. 11, pp. 9019–9026, 2002.
- [24] C. Wang, F. Grillot, V. I. Kovanis, J. D. Bodyfelt, and J. Even, "Modulation properties of optically injection-locked quantum cascade lasers," *Opt. Lett.*, vol. 38, no. 11, pp. 1975–1977, 2013.
- [25] G. Milovanovic and H. Kosina, "A semiclassical transport model for quantum cascade lasers based on the Pauli master equation," *J. Comput. Electron.*, vol. 9, nos. 3–4, pp. 211–217, 2010.
- [26] R. Terazzi and J. Faist, "A density matrix model of transport and radiation in quantum cascade lasers," *New J. Phys.*, vol. 12, no. 3, p. 033045, 2010.
- [27] T. Kubis, C. Yeh, P. Vogl, A. Benz, G. Fasching, and C. Deutsch, "Theory of nonequilibrium quantum transport and energy dissipation in terahertz quantum cascade lasers," *Phys. Rev. B*, vol. 79, no. 19, p. 195323, 2009.
- [28] A. Wacker, M. Lindskog, and D. O. Winge, "Nonequilibrium green's function model for simulation of quantum cascade laser devices under operating conditions," *IEEE J. Sel. Topics Quantum Electron.*, vol. 19, no. 5, pp. 1–11, Sep./Oct. 2013.
- [29] G. Beji, Z. Ikonić, C. A. Evans, D. Indjin, and P. Harrison, "Coherent transport description of the dual-wavelength ambipolar terahertz quantum cascade laser," *J. Appl. Phys.*, vol. 109, no. 1, p. 013111, 2011.
- [30] O. Baumgartner, Z. Stanojevic, and H. Kosina, "Efficient simulation of quantum cascade lasers using the Pauli master equation," in *Proc. Simulation Semiconductor Process. Devices (SISPAD)*, 2011, pp. 91–94.
- [31] E. S. Peer, F. van den Bergh, and A. Engelbrecht, "Using neighbourhoods with the guaranteed convergence PSO," in *Proc. IEEE Swarm Intell. Symp. (SIS)*, Apr. 2003, pp. 235–242.
- [32] Y. Shi and R. Eberhart, "A modified particle swarm optimizer," in *Proc. IEEE World Congr. Comput. Intell., Evol. Comput.*, May 1998, pp. 69–73.
- [33] C. Gmachl, F. Capasso, D. L. Sivco, and A. Y. Cho, "Recent progress in quantum cascade lasers and applications," *Rep. Progr. Phys.*, vol. 64, no. 11, pp. 1533–1601, 2001.
- [34] J. Faist, D. Hofstetter, M. Beck, T. Aellen, M. Rochat, and S. Blaser, "Bound-to-continuum and two-phonon resonance, quantum-cascade lasers for high duty cycle, high-temperature operation," *IEEE J. Quantum Electron.*, vol. 38, no. 6, pp. 533–546, Jun. 2002.
- [35] R. Graham and H. Haken, "Quantum theory of light propagation in a fluctuating laser-active medium," *Zeitschrift Phys.*, vol. 213, no. 5, pp. 420–450, 1968.



Mahdi Moradinab was born in Tehran, Iran, in 1982. He received the M.S. degree in electrical engineering from the University of Tehran, Tehran, in 2009. He is currently pursuing the Ph.D. degree in technical sciences with the Technische Universität Wien, Vienna, Austria. His research topics are numerical study of novel semiconductor devices, quantum transport in nanostructures, optical properties of nanostructures, and photonics.



Mahdi Pourfath was born in Tehran, Iran, in 1978. He received the B.S. and M.S. degrees in electrical engineering from the Sharif University of Technology, Tehran, in 2000 and 2002, respectively, and the Ph.D. degree in microelectronics from the Technische Universität Wien, Vienna, Austria, in 2007. He has authored or co-authored over 110 scientific publications and presentations, and authored one monograph. He is currently an Assistant Professor with the School of Electrical and Computer Engineering, University of Tehran, Tehran. He is also with the Institute of Microelectronics, Technische Universität Wien. His scientific interests include novel nanoelectronic devices and materials.



Hans Kosina (S'89–M'93) received the Dipl.Ing. degree in electrical engineering and the Ph.D. degree from the Technische Universität Wien, Vienna, Austria, in 1987 and 1992, respectively, and the Venia Docendi degree in microelectronics in 1998. For one year, he was with the Institute of Flexible Automation, Technische Universität Wien, where he is currently an Associate Professor with the Institute for Microelectronics. In Summer 1993, he was a Visiting Scientist with Motorola Inc., Austin, TX, USA, and in Summer 1999, he was a Visiting Faculty with Intel Corporation, Santa Clara, CA, USA. His current research interests include device modeling of semiconductor devices, nanoelectronic devices, organic semiconductors and optoelectronic devices, development of novel Monte Carlo algorithms for classical and quantum transport problems, and computer-aided engineering in ULSI technology.